



Nanocrystalline strain glass TiNiPt and its superelastic behaviorDaqiang Jiang ^{1,*}, Jiale An,¹ Yinong Liu,^{2,†} Zhiyuan Ma,¹ Fangfeng Liu,¹ Hong Yang,² Xiaobing Ren,^{3,4} Kaiyuan Yu,¹ Junsong Zhang,² Xiaohua Jiang,¹ Yang Ren ⁵ and Lishan Cui^{1,6,‡}¹State Key Laboratory of Heavy Oil Processing and Department of Materials Science and Engineering, China University of Petroleum, Beijing 102249, China²Department of Mechanical Engineering, The University of Western Australia, Perth, WA 6009, Australia³Frontier Institute of Science and Technology, and State Key Laboratory for Mechanical Behaviour of Materials, Xi'an Jiaotong University, Xi'an 710049, China⁴National Institute for Materials Science, Tsukuba 305-0047, Japan⁵X-ray Science Division, Argonne National Laboratory, Argonne, Illinois 60439, USA⁶Beijing Key Laboratory of Failure, Corrosion, and Protection of Oil/Gas Facilities, China University of Petroleum Beijing, Beijing 102249, China

(Received 6 May 2021; revised 23 June 2021; accepted 24 June 2021; published 6 July 2021; corrected 19 July 2021)

TiNi-based shape-memory alloys are known to exhibit a strain glass state under certain conditions, generally in the presence of high-density defects such as excess solute atoms or alloying elements, dislocations, and nanoprecipitates. In this paper, we report a strain glass transition in a nanocrystalline Ti₅₀Ni₃₅Pt₁₅ alloy. The nanocrystalline strain glass state is achieved by a combined effect of high-density grain boundaries and high concentration doping of Pt atoms in the B2 matrix. The nanocrystalline Ti₅₀Ni₃₅Pt₁₅ strain glass alloy showed a large near-complete progressive superelasticity with a recovery strain of about 6% and a low apparent Young's modulus of about 30 GPa in a wide temperature range of over 200 °C. *In situ* synchrotron x-ray diffraction measurement showed that the strain glass B2 [B2(SG)] phase experienced B2(SG)→R→B19 transformation upon loading and B19→B2(SG) upon unloading. The findings of this study provide insight for the development of nanocrystalline strain glass shape-memory alloys.

DOI: [10.1103/PhysRevB.104.024102](https://doi.org/10.1103/PhysRevB.104.024102)**I. INTRODUCTION**

“Strain glass” describes a special state of a crystalline metal matrix composed of a vast population and high density of nanodomains of lattice distortions in random orientations [1]. Such state occurs in alloys that generally exhibit martensitic transformations but when the transformations are suppressed by high densities of structural defects. These defects in high densities create very small interdefect distances on the order of several nanometers, which break down the long-range order of the crystalline matrix and severely impede mechanically the crystallographic lattice distortions of the otherwise thermodynamically favored martensitic transformation. This results in minuscule local lattice distortion strains, often beyond the detection of conventional lattice diffraction techniques, within a massive population of local nanodomains of random orientations, thus the strain glass state.

The strain glass state was first reported in some Ni-rich TiNi shape-memory alloys (SMAs) [2], containing high densities of third element atoms [3–8], dislocations [9], and nanoprecipitates [10,11]. Four main experimental characteristics are often used to verify the occurrence of strain glass state [2], including an invariance of average structure of

the parent phase (B2 for TiNi) with decreasing temperature, the frequency dependence of AC mechanical susceptibility obeying the Vogel-Fulcher relation, the breakdown of ergodicity or the existence of history dependence of physical properties (strain), and the presence of nanodomains of local lattice strains.

This strain glass state of martensitic transforming alloys provides them a unique mechanism for some novel properties that are absent in conventional alloys of more ordered and relaxed lattices, such as the Invar effect, Elinvar effect, large magnetostriction, small hysteresis, high damping, low modulus, and transformation pseudoelasticity over extraordinary wide temperature ranges [2–7,12–16].

It has been reported recently that the thermally induced B2→R and B2→B19' martensitic transformations can be suppressed in nanocrystalline TiNi-based alloys (containing high density of grain boundaries) formed by crystallization from an amorphous state through low-temperature annealing [17]. TEM studies reveal that the B19' martensite is fully suppressed in grains smaller than 60 nm and the R phase is suppressed when the grain size is further reduced to 15 nm even upon cooling to the cryogenic temperature [18]. The suppression of martensitic transformations in these alloys fulfills a prerequisite for achieving strain glass state [4,6,7,13], though grain-size reduction has generally not been considered an effective way to form strain glasses. This is largely due to the difficulty in achieving grain sizes small enough to reach the critical defect density (interdefect spacing) for forming

*dq80jiang@126.com

†yinong.liu@uwa.edu.au

‡lscai@cup.edu.cn

strain glasses and to have a high uniformity of these very small nanograins without abnormal growth. This often results in the local occurrence of B2→R transformation in the larger grains in these nanocrystalline TiNi alloys [18,19].

Ren *et al.* [20] studied the effect of Pd (a larger atom than both Ti and Ni) doping in causing the strain glass state in $\text{Ti}_{50}\text{Ni}_{50-x}\text{Pd}_x$. They found that Pd doping alone is insufficient to disrupt the long-range order of the B2 phase in $\text{Ti}_{50}\text{Ni}_{50-x}\text{Pd}_x$, but a slight increase of Ni content by 1 at. % changed $\text{Ti}_{49}\text{Ni}_{51-x}\text{Pd}_x$ into a strain glass state. This implies that a strain glass state is easier to achieve by codoping of multiple species, demonstrating the synergy between the different contributors. Considering the above, we may expect that doping of TiNi by a third element may help to increase the critical grains size, or increase the grain-size tolerance, for achieving the strain glass state in nanocrystalline TiNiX alloys. This will alleviate the materials processing difficulty in achieving uniform nanocrystalline microstructures. This study applied this concept and investigated the synergy between nanocrystallization and Pt doping on inducing the strain glass state in a $\text{Ti}_{50}\text{Ni}_{35}\text{Pt}_{15}$ SMA and its thermomechanical behavior.

II. EXPERIMENTAL PROCEDURE

A $\text{Ti}_{50}\text{Ni}_{35}\text{Pt}_{15}$ (at. %) ingot about 100 g in mass was prepared by vacuum arc melting from high-purity Ti (99.8 wt. %), Ni (99.9 wt. %) and Pt (99.95 wt. %) in an Ar atmosphere. The ingot was homogenized at 1050 °C for 12 h in a vacuum furnace and then hot rolled into a plate of 1.0 mm in thickness. Thin strips of 1.0 mm × 1.0 mm in cross section were cut from the plate along the rolling direction by means of electrical discharge wire cutting and then subjected to cold-wire drawing into thin wires of 0.23 mm in diameter in multiple steps with process annealing at 750 °C. The areal reduction of the last cold drawing was 79%.

The cold-drawn wire was in amorphous state, as confirmed by x-ray diffraction (XRD) measurement [21,22]. The crystallization behavior of the cold-drawn wire was measured using a TA Q20 differential scanning calorimeter (DSC) with a heating/cooling rate of 10 °C/min. The crystallization peak temperature was 480 °C. Consequently, all the nanocrystalline

samples were annealed at 480 °C for 10 min. Dynamic mechanical analysis (DMA) was carried out in tensile mode using a TA Q800 instrument with a cooling rate of 2 °C/min to characterize the strain glass transition with a constant displacement amplitude of 10 μm and in five frequencies (0.2, 1, 5, 10, and 20 Hz). The “zero-field cooling” (ZFC) and “field cooling” (FC) measurements were performed sequentially in two temperature cycles with a cooling rate of 5 °C/min by using a TA Q800 DMA unit. In this process, the sample was first cooled to −150 °C under zero stress. A load of 50 MPa was applied at this temperature and then the sample was heated to 300 °C under this stress. Then, the sample was cooled and heated with the same stress through the temperature cycle the second time. Electrical resistivity of the sample was measured by the four-probe method with a cooling/heating rate of 10 °C/min in vacuum.

The microstructure of the alloy wire was analyzed by means of transmission electron microscopy (TEM) using a Tecnai F20 microscope. The microstructure was characterized using the hollow-cone dark-field (HCDF) imaging method, which is suitable to form high image contrast for nanocrystalline microstructure [23]. *In situ* synchrotron high-energy x-ray diffraction (HEXRD) measurements were conducted at the 11-ID-C beamline of the Advanced Photon Source at Argonne National Laboratory, USA. HEXRD was used to investigate the structure and lattice strain evolutions of the alloy during tensile deformation. The x ray had a beam size of 0.4 mm × 0.4 mm and a wavelength of 0.0108 nm. The diffraction was generated in a transmission geometry. Tensile testing was carried out using a WDT-II tensile testing machine with a strain rate of $1 \times 10^{-3} \text{ s}^{-1}$.

III. RESULTS

A. Evidence of nanocrystalline strain glass state

Figure 1 shows a TEM analysis of the microstructure of the $\text{Ti}_{50}\text{Ni}_{35}\text{Pt}_{15}$ alloy wire after annealing at 480 °C for 10 min. Figure 1(a) is a HCDF micrograph of the sample generated using the (110)_{B2} diffraction ring. The inset is a selected area electron diffraction pattern. The sample was fully crystalline. Figure 1(b) shows the grain-size distribution of 1000 grains in the sample. The average grain size is ~13 nm.

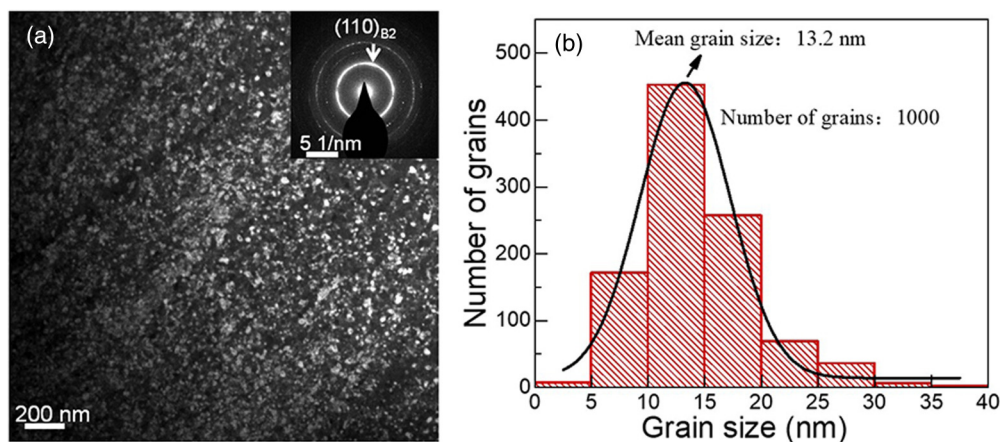


FIG. 1. Microstructure of the nanocrystalline $\text{Ti}_{50}\text{Ni}_{35}\text{Pt}_{15}$ alloy wire after annealing at 480 °C for 10 min. (a) A hollow-cone dark-field image, revealing the nanocrystallinity of the sample. (b) Grain-size distribution as determined from the HCDF image.

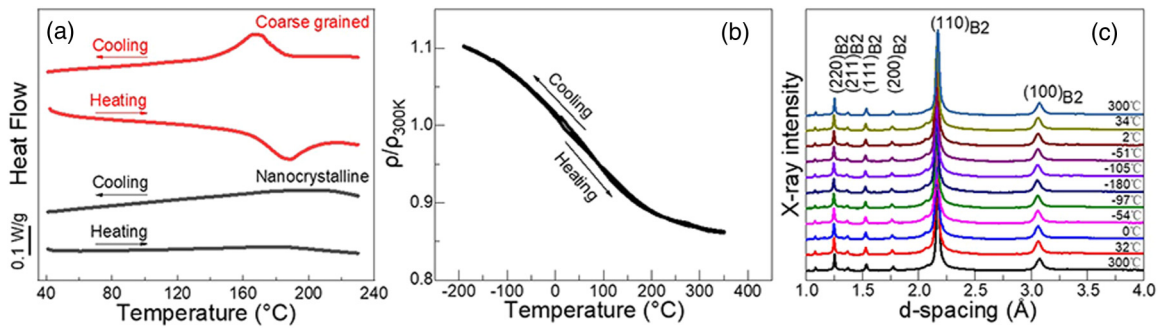


FIG. 2. The transformation behavior and structure evolution of the nanocrystalline $\text{Ti}_{50}\text{Ni}_{35}\text{Pt}_{15}$ sample (a) DSC curves of the nanocrystalline $\text{Ti}_{50}\text{Ni}_{35}\text{Pt}_{15}$ sample and a coarse-grained $\text{Ti}_{50}\text{Ni}_{35}\text{Pt}_{15}$ sample annealed at 700°C for 10 min. (b) Normalized (at 300 K) electrical resistivity-temperature curve of the nanocrystalline $\text{Ti}_{50}\text{Ni}_{35}\text{Pt}_{15}$ alloy. (c) XRD patterns of the nanocrystalline $\text{Ti}_{50}\text{Ni}_{35}\text{Pt}_{15}$ alloy at different temperatures.

Figure 2 shows the transformation behavior and structure evolution of the nanocrystalline $\text{Ti}_{50}\text{Ni}_{35}\text{Pt}_{15}$ sample. Figure 2(a) shows the transformation behaviors of the nanocrystalline $\text{Ti}_{50}\text{Ni}_{35}\text{Pt}_{15}$ alloy and a coarse-grained $\text{Ti}_{50}\text{Ni}_{35}\text{Pt}_{15}$ sample prepared by annealing at 700°C for 10 min. The nanocrystalline $\text{Ti}_{50}\text{Ni}_{35}\text{Pt}_{15}$ wire showed no transformation within the temperature range of $40\text{--}220^\circ\text{C}$. This is different from previously reported observations, in which nanocrystalline TiNi alloys of similar grain sizes exhibited clear B2-R transformation at about 50°C [18,19]. In comparison, the coarse-grained sample showed a clear reversible B2→B19 martensitic transformation at around 180°C during heating and cooling.

Figure 2(b) shows a normalized electrical resistivity (ER) curve of the nanocrystalline $\text{Ti}_{50}\text{Ni}_{35}\text{Pt}_{15}$ sample during heating and cooling. It can be seen that the ER started to increase at 350°C upon cooling and continued to -180°C . Upon heating the sample showed the reverse process without a thermal hysteresis. Such abnormal increase of ER with lowering temperature in TiNi has been attributed to the formation and growth of “R-like” nanodomains within the B2 matrix [24]. The onset temperature for the abnormal increase of ER, de-

noted as T_{nd} [8], indicates that the nanodomains begin to form as high as 350°C in the nanocrystalline $\text{Ti}_{50}\text{Ni}_{35}\text{Pt}_{15}$ alloy. This is much higher than the previously reported T_{nd} of 80°C in strain glass TiNi [25] and 100°C in strain glass TiPdFe [11].

Figure 2(c) shows an *in situ* high-energy synchrotron XRD measurement of the nanocrystalline $\text{Ti}_{50}\text{Ni}_{35}\text{Pt}_{15}$ sample at different temperatures. It is seen that the sample remained in B2 structure over the entire temperature range from 300 to -180°C . This is consistent with the characteristic that strain glass TiNi maintains its B2 structure [13].

Figure 3 shows a dynamic mechanical analysis of the nanocrystalline $\text{Ti}_{50}\text{Ni}_{35}\text{Pt}_{15}$ sample. Figure 3(a) plots the storage modulus curves of the sample at different frequencies. It is seen that the storage modulus decreased with decreasing temperature from 90°C and reached a minimum at about $50\text{--}60^\circ\text{C}$, and then started to increase with decreasing temperature. The temperature of the lowest storage modulus is identified as the T_g temperature of the alloy at which the matrix transformed from an unfrozen strain glass state into a frozen strain glass state on cooling [3]. The inset in Fig. 3(a) shows the Vogel-Fulcher fitting curve of T_g . It is

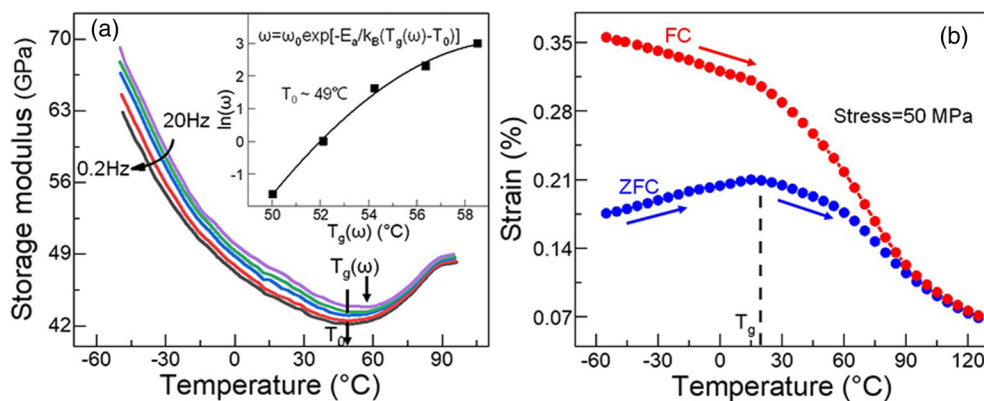


FIG. 3. Dynamic mechanical properties of the nanocrystalline $\text{Ti}_{50}\text{Ni}_{35}\text{Pt}_{15}$. (a) Effect of temperature on storage modulus of the nanocrystalline $\text{Ti}_{50}\text{Ni}_{35}\text{Pt}_{15}$ at different frequencies. (b) ZFC/FC curves of the nanocrystalline $\text{Ti}_{50}\text{Ni}_{35}\text{Pt}_{15}$. The sample was cooled to -150°C under zero applied force (denoted zero-field cooling, or ZFC). Then a tensile stress of 50 MPa was applied and the sample was heated to 300°C under this stress, presented as the ZFC curve in the figure. Then the sample was cooled to -150°C under the 50-MPa tensile stress, denoted the field cooling and then heated to 300°C again under the same stress, presented as the FC curve in the figure. For each curve, the effect of thermal dilation of the sample has been removed by subtracting the strain-temperature curve measured upon the first cooling under zero stress.

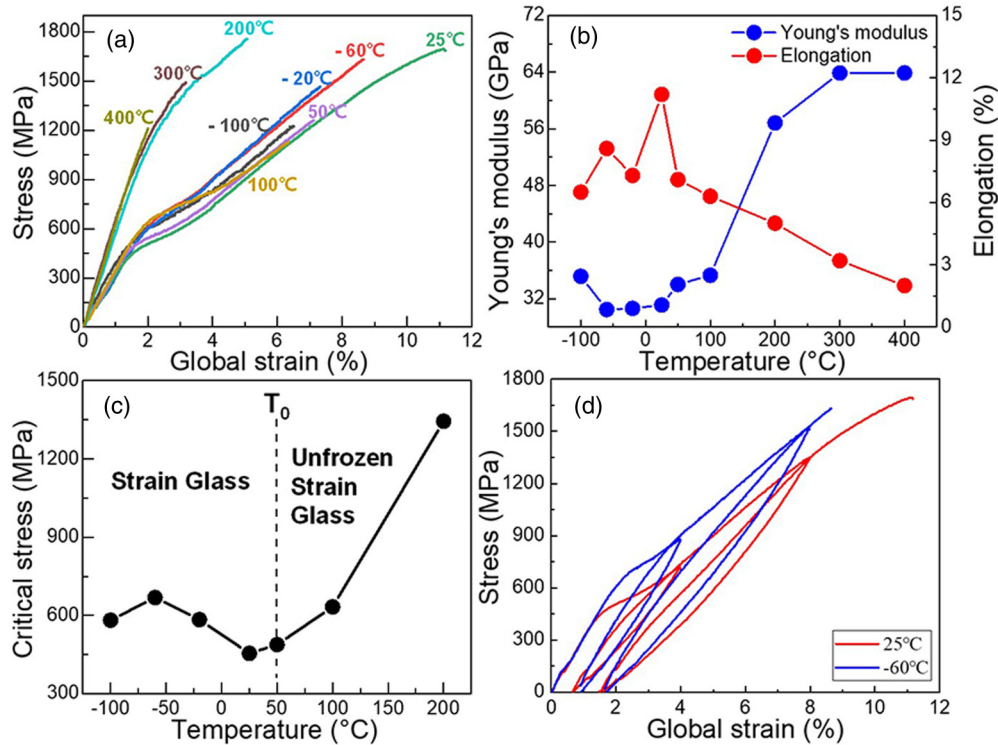


FIG. 4. Mechanical behavior of the nanocrystalline $\text{Ti}_{50}\text{Ni}_{35}\text{Pt}_{15}$ alloy. (a) Tensile stress-strain curves at different temperatures. (b) Effect of testing temperature on the apparent Young modulus and elongation. (c) Temperature dependence of the critical stress for stress-induced transformation, (d) Progressive deformation curves at the room temperature and -60°C .

seen that T_g increased with increasing the frequency ω , and the dependence obeys a Vogel-Fulcher relationship [26] $\omega = \omega_0 \exp[-E_a/k_B(T_g(\omega) - T_0)]$, where ω_0 , E_a , k_B , and T_0 are the frequency prefactor, activation energy, Boltzmann constant, and ideal freezing temperature of the strain glass transition, respectively. The ideal freezing temperature T_0 is determined to be $\sim 49^\circ\text{C}$ from the fitting curve. Another major feature of strain glass transition is the nonergodicity, which is demonstrated by measuring the historical dependence of strain under a small external stress.

Figure 3(b) shows strain-temperature measurements of a nanocrystalline $\text{Ti}_{50}\text{Ni}_{35}\text{Pt}_{15}$ sample upon heating over two measurement cycles. In the first measurement cycle the sample was cooled to -150°C under zero applied force (denoted zero-field cooling, or ZFC) to produce a randomly oriented frozen strain nanodomain structure. This first cooling curve also serves as the record of the effect of thermal expansion of the sample for calibration. Then a tensile stress of 50 MPa was applied and the sample was heated to 300°C under this stress, presented as the ZFC curve in the figure. In the second measurement cycle, the sample was cooled to -150°C under the 50-MPa tensile stress to form an oriented frozen strain nanodomain structure, denoted the field cooling (FC). The sample was then heated to 300°C again under the same stress, presented as the FC curve in the figure. For each curve, the effect of thermal dilation of the sample has been removed by subtracting the strain-temperature curve measured upon the first cooling under zero stress. The ZFC sample showed an initial increase of strain from -60 to 20°C . This is attributed to a stress-assisted strain reorientation of the randomly oriented

nanodomains formed under the ZFC condition, apparently due to thermal relaxation (unfreezing) upon heating. This caused a large deviation between the two curves at below T_g , revealing a strong nonergodicity of the straining process. This is similar to the ZFC/FC curves of spin glasses and ferroelectric relaxors [27,28], and has been used as evidence of the freezing of a strain glass phase [3,13].

B. Mechanical behavior of nanocrystalline strain glass $\text{Ti}_{50}\text{Ni}_{35}\text{Pt}_{15}$

Figure 4 shows the mechanical behavior of the nanocrystalline $\text{Ti}_{50}\text{Ni}_{35}\text{Pt}_{15}$ alloy. Figure 4(a) presents the tensile stress-strain curves at different temperatures. The alloy exhibited an increasing strain hardening between $2 \sim 4\%$ strain, implying a stress-induced transformation. At above 200°C , the alloy deformed largely via plastic deformation. Figure 4(b) plots the apparent Young modulus and the elongation of the samples tested at different temperatures. It is seen that the alloy exhibited the highest elongation of 11% at the room temperature, which deteriorated on both heating and cooling. The apparent Young modulus was 67 GPa at above 300°C , decreased with decreasing temperature to reach a minimum of 30 GPa at $25 \sim -60^\circ\text{C}$, and then increased upon further cooling. The decrease of the elastic modulus implies the participation of nonelastic deformation during this early stage of deformation, e.g., a stress-induced phase transformation. Similar observations have also been reported in the literature. Fukuda *et al.* [29] reported that the apparent Young modulus of the B2 austenite decreased with decreasing temperature in $\text{Ti}_{50}\text{Ni}_{44}\text{Fe}_6$ and attributed the observation to the occurrence

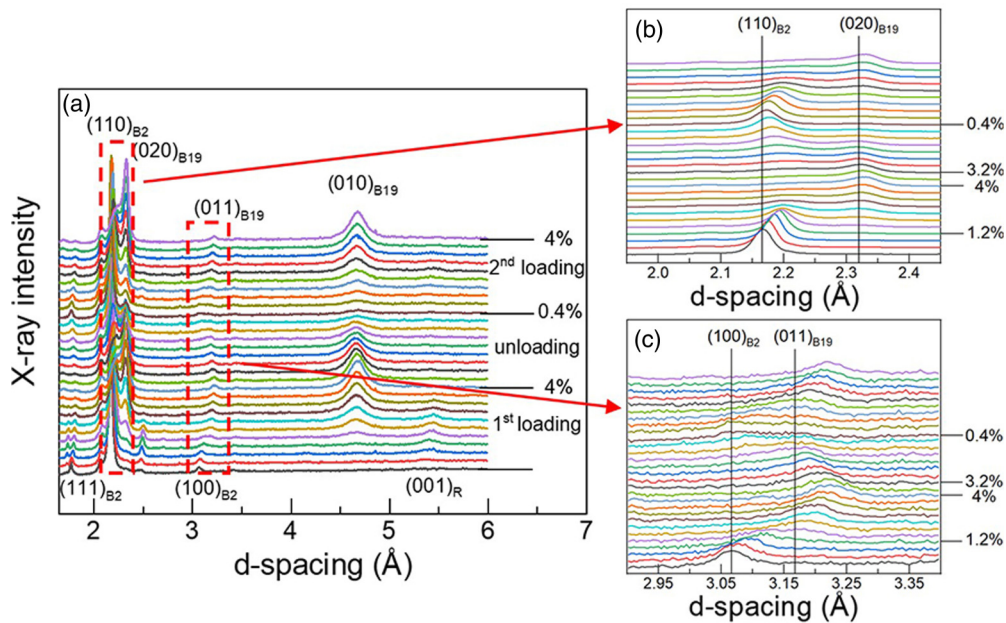


FIG. 5. *In situ* XRD analysis of the transformation behavior of the nanocrystalline $\text{Ti}_{50}\text{Ni}_{35}\text{Pt}_{15}$ alloy during tensile deformation. (a) 1D XRD spectra integrated over $\pm 5^\circ$ azimuthal angle of the loading direction from the 2D XRD patterns measured by synchrotron high-energy XRD. (b), (c) Enlarged views of sections of the diffraction patterns identified by the boxes in (a).

of the incommensurate-commensurate transformation in the alloy. Šittner *et al.* [30] observed a significant decrease of the apparent Young modulus from 70 to 20 GPa associated with the stress-induced B2-R phase transformation during the apparent linear stage of deformation.

Figure 4(c) shows the effect of temperature on the critical stress for stress-induced martensitic transformation. The critical stress was estimated as the apparent “yielding” point using the conventional tangent method. The critical stress decreased rapidly with decreasing temperature from 100 to 25 °C and then increased with further decreasing the temperature. This is different from the conventional Clausius-Clapeyron relationship for stress-induced martensitic transformations [31], but similar to that of $\text{Ni}_{51.5}\text{Ti}_{48.5}$ and $\text{Ni}_{45}\text{Co}_5\text{Mn}_{36}\text{In}_{14}$ alloys [15,32]. The increase of the critical stress for stress-induced martensitic transformation upon cooling was attributed to an increased stress hysteresis.

Figure 4(d) shows the stress-strain curves of two samples tested at two different temperatures, both within the frozen strain glass state range of the alloy. The alloy was superelastic at both the room temperature and -60°C . The superelastic strain (recovered strain) reached was 6.35% at the room temperature and 6.27% at -60°C , after deforming to 8% strain. It has been reported that coarse-grained TiNi exhibited superelasticity in the unfrozen strain glass state above T_0 and shape-memory effect in the frozen strain glass state below T_0 [13]. However, this nanocrystalline $\text{Ti}_{50}\text{Ni}_{35}\text{Pt}_{15}$ alloy is superelastic in the frozen strain glass state below its T_0 . This may be related to its small grain sizes. It is also evident that the stress-induced transformation occurred over a progressively wide stress window, instead of over a stress plateau. This indicates a complex deformation process. The actual deformation mechanisms may include elastic deformation of B2(SG), lattice distortion of the strain glass nanodomains,

stress-induced B2→R→B19 and B2→B19 transformations, and plastic deformation upon loading, and elastic recovery, pseudoelastic reverse B19→B2(SG) transformation, and lattice distortion recovery of the strain glass nanodomains. The lattice distortion of the strain glass nanodomains is expected to commence at very low stress levels and its participation gives the very low apparent Young modulus (~ 30 GPa) of the alloy.

Figure 5 shows an *in situ* high-energy synchrotron XRD analysis of the nanocrystalline $\text{Ti}_{50}\text{Ni}_{35}\text{Pt}_{15}$ alloy during two tensile deformation cycles to 4% strain. Stress-strain curves of the sample during *in situ* synchrotron XRD test at the room temperature (25 °C) is the same as that presented in Fig. 4(d). The XRD measurement was performed at a step size of 0.2% strain during the deformation with a stopover time of 10 s to collect the two-dimensional diffraction patterns. Figure 5(a) shows 1D XRD patterns for the wire axial direction obtained by integrating the 2D synchrotron XRD within $\pm 5^\circ$ about the wire axial direction. In order to make it easier to recognize, the pattern of every 0.4% strain was used. Some landmark strains are indicated on the side of the figure to deformation stages of the first loading, unloading, and the second loading. The diffraction peaks are indexed based on standard crystalline structures of the phases. The lattice parameter of the B2 phase is $a = 3.015 \text{ \AA}$. The lattice parameters of the rhombohedral R phase are $a = 7.257 \text{ \AA}$, $b = 7.257 \text{ \AA}$, $c = 5.383 \text{ \AA}$, $\alpha = \beta = 90^\circ$, and $\gamma = 120^\circ$. The lattice parameters of the orthogonal B19 phase are $a = 2.8000 \text{ \AA}$, $b = 4.6310 \text{ \AA}$, $c = 4.1900 \text{ \AA}$, $\alpha = \beta = \gamma = 90^\circ$.

It is worth noting from Fig. 5(a) that the $(001)_R$ diffraction peak appeared immediately after the tensile deformation (0.4% strain) prior to the emergence of the $(011)_{B19}$ diffraction peak and then disappeared gradually upon further loading. This indicates that the sample underwent a stress-induced B2→R→B19 transformation upon loading. This is

similar to the TiNiFe strain glass alloy [29,33], in which a stress-induced B2(SG) \rightarrow R transformation was observed. This may explain the reason that the apparent Young modulus was low at room temperature since the immediate occurrence of the transformation during tensile deformation. During unloading, the B19 \rightarrow B2 transformation was observed, without the reverse B2 \rightarrow R transformation. During the second loading, the sample underwent the stress-induced B2 \rightarrow R \rightarrow B19 transformation again, only the intensity of (001)_R diffraction peak was weaker than that of the first loading.

Figure 5(b) shows an enlarged view of the section of the diffraction pattern between 2.0 and 2.4-Å d spacing, where (110)_{B2} and (020)_{B19} diffractions are visible. The two vertical lines indicate the positions of the respective diffraction peaks under stress-free conditions. It is seen that upon loading the (110)_{B2} peak shifted gradually to higher d -spacing values, indicating elastic elongation in the loading direction. At 1.2% strain, the (110)_{B2} peak gradually lowered in intensity and the (020)_{B19} peak emerged, indicating the stress-induced B2 \rightarrow B19 phase transformation. The (110)_{B2} peak did not disappear completely until 4% strain, from which the unloading commenced. Upon unloading, the reverse B19 \rightarrow B2 phase transformation occurred between 3.2 and 0.4% strains. It is also apparent that the newly formed B2 phase continued to contract in the axial direction upon unloading.

Similarly, Fig. 5(c) shows an enlarged view of the section between 2.95 and 3.35-Å d spacing, where (100)_{B2} and (011)_{B19} diffractions are visible. The two vertical lines indicate the positions of the respective diffraction peaks under stress-free conditions. Whereas the stress-induced B2 \rightarrow B19 forward transformation upon loading and the B19 \rightarrow B2 reverse transformation upon unloading can also be clearly recognized, the strain ranges of the transformations are much less definitive. Instead, the (100)_{B2} peak appears to evolve into the (011)_{B19} peak continuously. However, this does not mean a gradual lattice distortion of the B2 phase into the B19 martensite, which is a first-order phase transformation, but a coincidence of the continuous elastic deformation of the B2 and the continuous elastic deformation of the martensite after its appearance. This is obvious on the stress-strain curve shown in Fig. 4(d), where the stress-induced martensitic transformation occurred progressively with a continuously increasing stress. Such a progressive transformation is also evident in Fig. 5(b), where (110)_{B2} did not disappear completely until 4% strain whereas the (020)_{B19} peak appeared at 1.2% strain.

IV. DISCUSSION

A. T_0 temperature of nanocrystalline strain glass Ti₅₀Ni₃₅Pt₁₅

The T_0 temperature is the temperature of the glass transition (T_g) from an unfrozen state to the frozen state of a strain glass matrix at 0 Hz, as determined by extrapolating the T_g measured at different frequencies. Considering that M_s is the temperature of the martensitic transformation which has been suppressed, it is obvious that $T_0 < M_s$ for the alloy [34]. The T_0 temperature for strain glass transition has been reported to be generally in the range of $-100\sim-150$ °C for binary Ni-rich TiNi alloys [8], and close to the room temperature for Cr-doped TiPd high-temperature SMAs [4]. The M_s temper-

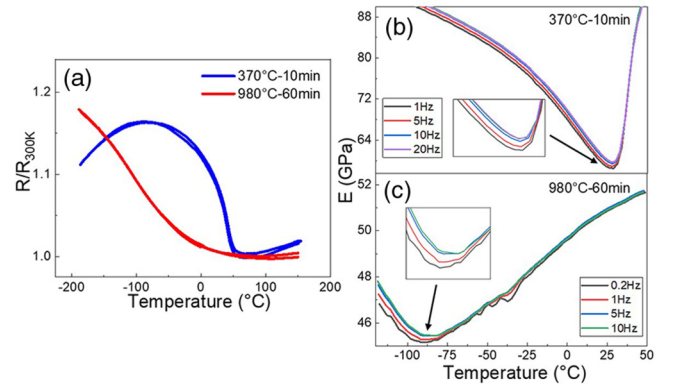


FIG. 6. The transformation behavior of the nanocrystalline and coarse-grained Ni_{51.5}Ti_{48.5} alloys. (a) Normalized electrical resistivity curves of a nanocrystalline sample and a solid solution treated coarse-grained sample of Ni_{51.5}Ti_{48.5}. Dynamic mechanical properties of the nanocrystalline Ni_{51.5}Ti_{48.5} (b) and the solid solution treated coarse-grained Ni_{51.5}Ti_{48.5} (c).

ature of the coarse-grained Ti₅₀Ni₃₅Pt₁₅ alloy is measured to be 180 °C, as shown in Fig. 2(a). This leads to the higher T_0 temperature of 49 °C in the nanocrystalline Ti₅₀Ni₃₅Pt₁₅ strain glass alloy as compared to the usual Ni-rich NiTi alloys.

B. The cause of strain glass state of the nanocrystalline Ti₅₀Ni₃₅Pt₁₅ alloy

It is clear above that the nanocrystalline Ti₅₀Ni₃₅Pt₁₅ alloy is in strain glass state. To help identify the main cause of the strain glass state, a comparative experiment was conducted on a nanocrystalline Ni_{51.5}Ti_{48.5} alloy, which is well known to be in strain glass state in the solid solution state. The nanocrystalline Ni_{51.5}Ti_{48.5} alloy was obtained by the same cold-wire drawing and low-temperature crystallization annealing process as used for the nanocrystalline Ti₅₀Ni₃₅Pt₁₅ alloy, except that the crystallization temperature was 370 °C due to its lower crystallization peak temperature.

Figure 6 shows the thermal analyses of the transformation behavior of a Ni-rich TiNi alloy. Figure 6(a) shows a comparison of the electrical resistance-temperature curves of a nanocrystalline Ni_{51.5}Ti_{48.5} sample and a coarse-grained sample of the same alloy. The nanocrystalline Ni_{51.5}Ti_{48.5} sample showed an obvious B2-R phase transformation at 20–50 °C. In comparison, the coarse-grained sample showed a continuous increase of the electrical resistance with decreasing temperature, a typical behavior of the strain glass transition. Figure 6(b) shows the dynamic mechanical behavior of the nanocrystalline Ni_{51.5}Ti_{48.5} sample, which also manifested the occurrence of the B2-R transformation. It is also evident in the inset that there is no frequency dependence of critical value of the storage modulus, implying that it is associated with the phase transformation and not the strain glass transition. Figure 6(c) shows the dynamic mechanical behavior of the coarse-grained Ni_{51.5}Ti_{48.5} sample. The critical temperature of the storage modulus exhibited a clear frequency dependence, signaling the strain glass state of the alloy.

In summary, the comparative study demonstrates that the nanocrystalline Ni_{51.5}Ti_{48.5} alloy is not in strain glass state

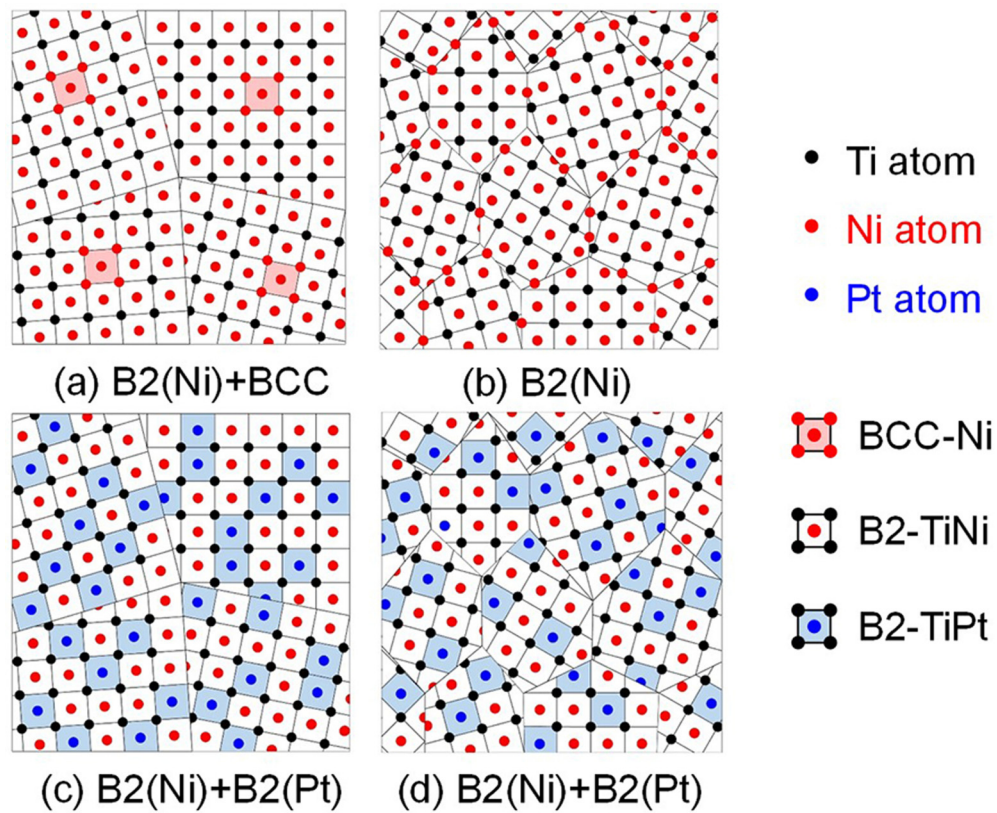


FIG. 7. Schematic illustrations of the unit-cell configurations in (a) coarse-grained Ni-rich TiNi alloy, (b) nanocrystalline Ni-rich TiNi alloy, (c) coarse-grained $\text{Ti}_{50}\text{Ni}_{35}\text{Pt}_{15}$ alloy, and (d) nanocrystalline $\text{Ti}_{50}\text{Ni}_{35}\text{Pt}_{15}$ alloy.

but the coarse-grained $\text{Ni}_{51.5}\text{Ti}_{48.5}$ alloy is. In comparison, the nanocrystalline $\text{Ti}_{50}\text{Ni}_{35}\text{Pt}_{15}$ alloy is in strain glass state but the coarse-grained alloy is not. A possible microscopic origin of the observed macroscopic behavior is explained as follows, and expressed in Fig. 7. In the coarse-grained Ni-rich $\text{Ni}_{51.5}\text{Ti}_{48.5}$, the excess Ni atoms form effectively body-centered cubic (bcc) unit cells within the B2 matrix, as shown in Fig. 7(a). Apparently, the presence of these all-Ni bcc unit cells in the matrix disrupts the long-range B2 ordering and causes the strain glass state in the coarse-grained $\text{Ni}_{51.5}\text{Ti}_{48.5}$. Given the alloy composition, there are 1.5 Ni-bcc unit cells for every 48.5 TiNi-B2 unit cells, i.e., they count for 3% of all the unit cells. This leaves an average inter-bcc cell distance of 3.2 unit cells, or about 1 nm. Such B2-bcc configuration is apparently sufficient to suppress the martensitic transformations and causing the strain glass state in the alloy. In a nanocrystalline matrix, on the other hand, the excess Ni atoms are mostly accommodated within the grain boundaries due to their higher solubility for solute atoms, as schematically illustrated in Fig. 7(b). This reduces the degree of off-stoichiometry for the B2 nanograins, leaving the grain composed of pure TiNi-B2 unit cells, thus the absence of the strain glass state.

For the $\text{Ti}_{50}\text{Ni}_{35}\text{Pt}_{15}$ alloy, the composition is “equiatomic” between Ti and (Ni, Pt) for the B2 structure. Therefore, the matrix can be considered to be composed of two types of B2 unit cells, i.e., TiNi-B2 [B2(Ni)] and TiPt-B2 [B2(Pt)], in 70% and 30% proportions, as expressed in Fig. 7(c). The absence of

a strain glass state in the coarse-grained $\text{Ti}_{50}\text{Ni}_{35}\text{Pt}_{15}$ implies that the B2(Ni)-B2(Pt) combination is a weak disruption of the B2 ordering and is insufficient to suppress the martensitic transformation. In a nanocrystalline matrix, the equiatomic nature implies that there is no grain-boundary segregation of any element and the matrix remains in B2(Ni)-B2(Pt) combination. With the additional contribution of the large amount of grain boundaries, the matrix resistance to the martensitic transformation is sufficient to cause the strain glass state, as expressed in Fig. 7(d). It is to be stated that, whereas clearly presenting a logical argument, this theory of the original of strain glass is yet to be directly proven, either experimentally by determining the atomic positioning in with the matrix or theoretical calculations by means of density-functional theories or molecular-dynamics simulation.

V. CONCLUSIONS

The main findings of this study may be summarized as below.

- (1) The nanocrystalline $\text{Ti}_{50}\text{Ni}_{35}\text{Pt}_{15}$ alloy is in strain glass state. The T_0 temperature of the nanocrystalline strain glass $\text{Ti}_{50}\text{Ni}_{35}\text{Pt}_{15}$ alloy is about 50°C , which is the highest among all the TiNi-based strain glass alloys to date.
- (2) The nanocrystalline strain glass $\text{Ti}_{50}\text{Ni}_{35}\text{Pt}_{15}$ exhibited a B2 \rightarrow R \rightarrow B19 superelasticity with a strain recovery exceeding 6% at room temperature and -60°C , a temperature 100°C

below T_0 . The nanocrystalline strain glass $\text{Ti}_{50}\text{Ni}_{35}\text{Pt}_{15}$ also exhibited a low apparent Young modulus of ~ 30 GPa.

(3) The strain glass state in $\text{Ti}_{50}\text{Ni}_{35}\text{Pt}_{15}$ is achieved by the combined effects of Pt substitution for Ni and nanocrystallinity, neither being sufficient alone. A possible microscopic origin of the formation of strain glass state is that the B2-bcc matrix unit-cell configuration in doped nonstoichiometric alloys is more effective in causing the strain glass state than the B2(1)-B2(2) configuration in substitutional stoichiometric alloys.

ACKNOWLEDGMENTS

The authors gratefully acknowledge the financial support of the National Natural Science Foundation of China (Grants No. 51731010, No. 51831006, and No. 51971243), and the financial support of Australian Research Council in Grants No. DP180101955 and No. DP190102990. This research used resources of the Advanced Photon Source, a U.S. Department of Energy (DOE) Office of Science User Facility operated for the DOE Office of Science by Argonne National Laboratory under Contract No. DE-AC02-06CH11357.

- [1] C. Liu, Y. Ji, and X. Ren, Strain glass and novel properties, *Shape Mem. Superelasticity* **5**, 299 (2019).
- [2] S. Sarkar, X. Ren, and K. Otsuka, Evidence for Strain Glass in the Ferroelastic-Martensitic System $\text{Ti}_{(50-x)}\text{Ni}_{(50+x)}$, *Phys. Rev. Lett.* **95**, 205702 (2005).
- [3] Y. Wang, X. Ren, K. Otsuka, and A. Saxena, Evidence for broken ergodicity in strain glass, *Phys. Rev. B* **76**, 132201 (2007).
- [4] Y. Zhou, D. Xue, X. Ding, K. Otsuka, J. Sun, and X. Ren, High temperature strain glass in $\text{Ti}_{50}\text{Pd}_{50-x}\text{Cr}_x$ alloy and the associated shape memory effect and superelasticity, *Appl. Phys. Lett.* **95**, 151906 (2009).
- [5] Y. Wang, Y. Zhou, J. Zhang, X. Ding, S. Yang, X. Song, X. Ren, and K. Otsuka, Evolution of the relaxation spectrum during the strain glass transition $\text{Ti}_{48.5}\text{Ni}_{51.5}$ of alloy, *Acta Mater.* **58**, 4723 (2010).
- [6] Y. Zhou, D. Xue, X. Ding, Y. Wang, J. Zhang, Z. Zhang, D. Wang, K. Otsuka, J. Sun, and X. Ren, Strain glass in doped $\text{Ti}_{50}\text{Ni}_{50-x}\text{D}_x$ ($D = \text{Co}, \text{Cr}, \text{Mn}$) alloys: Implication for the generality of strain glass in defect-containing ferroelastic systems, *Acta Mater.* **58**, 5433 (2010).
- [7] D. Wang, Z. Zhang, J. Zhang, Y. Zhou, Y. Wang, X. Ding, Y. Wang, and X. Ren, Strain glass in Fe-doped Ti-Ni, *Acta Mater.* **58**, 6206 (2010).
- [8] Z. Zhang, Y. Wang, D. Wang, Y. Zhou, K. Otsuka, and X. Ren, Phase diagram of $\text{Ti}_{50-x}\text{Ni}_{50+x}$: Crossover from martensite to strain glass, *Phys. Rev. B* **81**, 224102 (2010).
- [9] J. Zhang, D. Xue, X. Cai, X. Ding, X. Ren, and J. Sun, Dislocation induced strain glass in $\text{Ti}_{50}\text{Ni}_{45}\text{Fe}_5$ alloy, *Acta Mater.* **120**, 130 (2016).
- [10] Y. Ji, X. Ding, T. Lookman, K. Otsuka, and X. Ren, Heterogeneities and strain glass behavior: Role of nanoscale precipitates in low-temperature-aged $\text{Ti}_{48.7}\text{Ni}_{51.3}$ alloys, *Phys. Rev. B* **87**, 104110 (2013).
- [11] S. Ren, C. Liu, X. Chen, Y. Hao, and X. Ren, Strain glass by aging in Ti-Pd-Fe shape memory alloys, *Scr. Mater.* **177**, 11 (2020).
- [12] D. Wang, Y. Wang, Z. Zhang, and X. Ren, Modeling Abnormal Strain States in Ferroelastic Systems: The Role of Point Defects, *Phys. Rev. Lett.* **105**, 205702 (2010).
- [13] Y. Wang, X. Ren, and K. Otsuka, Shape Memory Effect and Superelasticity in a Strain Glass Alloy, *Phys. Rev. Lett.* **97**, 225703 (2006).
- [14] S. Ren, D. Xue, Y. Ji, X. Liu, S. Yang, and X. Ren, Low-Field Triggered Large Magnetostriction in Iron-Palladium Strain Glass Alloys, *Phys. Rev. Lett.* **119**, 125701 (2017).
- [15] K. Niitsu, T. Omori, and R. Kainuma, Stress-induced transformation behaviors at low temperatures in Ti-51.8Ni (at.%) shape memory alloy, *Appl. Phys. Lett.* **102**, 231915 (2013).
- [16] F. Y. Qin, W. L. Xiao, F. S. Lu, Y. C. Ji, X. Q. Zhao, and X. B. Ren, *J. Mater. Sci. Technol.* **35**, 396 (2019).
- [17] T. Waitz, V. Kazykhanov, and H. P. Karnthaler, Martensitic phase transformations in nanocrystalline NiTi studied by TEM, *Acta Mater.* **52**, 137 (2004).
- [18] X. Shi, L. Cui, D. Jiang, C. Yu, F. Guo, M. Yu, Y. Ren, and Y. Liu, Grain size effect on the R-phase transformation of nanocrystalline NiTi shape memory alloys, *J. Mater. Sci.* **49**, 4643 (2014).
- [19] T. Wang, Z. Ma, X. Rao, D. Jiang, Y. Ren, Y. Liu, K. Yu, and L. Cui, Temperature-dependence of superelastic stress in nanocrystalline NiTi with complete transformation capability, *Intermetallics* **127**, 106970 (2020).
- [20] S. Ren, C. Zhou, D. Xue, D. Wang, J. Zhang, X. Ding, K. Otsuka, and X. Ren, Sandwich-like strain glass phase diagram of $\text{Ti}_{49}\text{Ni}_{51-x}\text{Pd}_x$, *Phys. Rev. B* **94**, 214112 (2016).
- [21] B. Feng, X. Kong, S. Hao, Y. Liu, Y. Yang, H. Yang, F. Guo, D. Jiang, T. Wang, Y. Ren, and L. Cui, In-situ synchrotron high energy X-ray diffraction study of micro-mechanical behaviour of R phase reorientation in nanocrystalline NiTi alloy, *Acta Mater.* **194**, 565 (2020).
- [22] C. Yu, B. Aoun, L. Cui, Y. Liu, H. Yang, X. Jiang, S. Cai, D. Jiang, Z. Liu, and D. E. Brown, Synchrotron high energy X-ray diffraction study of microstructure evolution of severely cold drawn NiTi wire during annealing, *Acta Mater.* **115**, 35 (2016).
- [23] B. Yao, T. Sun, A. Warren, H. Heinrich, K. Barmak, and K. R. Coffey, High contrast hollow-cone dark field transmission electron microscopy for nanocrystalline grain size quantification, *Micron* **41**, 177 (2010).
- [24] Y. Murakami and D. Shindo, Changes in microstructure near the R-phase transformation in $\text{Ti}_{50}\text{Ni}_{48}\text{Fe}_2$ studied by in-situ electron microscopy, *Philos. Mag. Lett.* **81**, 631 (2001).
- [25] S. Kustov, D. Salas, E. Cesari, R. Santamarta, D. Mari, and J. V. Humbeeck, Structural anelasticity, elasticity and broken ergodicity in Ni-Ti shape memory alloys, *Acta Mater.* **73**, 275 (2014).
- [26] J. C. Qiao and J. M. Pelletier, *J. Mater. Sci. Technol.* **30**, 523 (2014).
- [27] N. Gayathri, A. K. Raychaudhuri, S. K. Tiwary, R. Gundakaram, A. Arulraj, and C. N. R. Rao, Electrical transport, magnetism, and magnetoresistance in ferromagnetic

- oxides with mixed exchange interactions: A study of the $\text{La}_{0.7}\text{Ca}_{0.3}\text{Mn}_{1-x}\text{Co}_x\text{O}_3$ system, *Phys. Rev. B* **56**, 1345 (1997).
- [28] Q. Tan, J. F. Li, and D. Viehland, Role of potassium comodification on domain evolution and electrically induced strains in La modified lead zirconate titanate ferroelectric ceramics, *J. Appl. Phys.* **88**, 3433 (2000).
- [29] T. Fukuda, G. Yamasaki, H. Yoshinobu, and T. Kakeshita, Mechanical properties of the R-phase and the commensurate phase under [111] tensile stress in iron-doped titanium-nickel alloys, *Mater. Trans.* **57**, 278 (2016).
- [30] P. Šittner, M. Landa, P. Lukas, and V. Novak, R-phase transformation phenomena in thermomechanically loaded NiTi polycrystals, *Mech. Mater.* **38**, 475 (2006).
- [31] P. Wollants, M. De Bonte, and J. R. Roos, A thermodynamic analysis of the stress-induced martensitic transformation in a single crystal, *Z. Metallkd.* **70**, 113 (1979).
- [32] K. Niitsu, X. Xu, R. Y. Umetsu, and R. Kainuma, Stress-induced transformations at low temperatures in a $\text{Ni}_{45}\text{Co}_5\text{Mn}_{36}\text{In}_{14}$ metamagnetic shape memory alloy, *Appl. Phys. Lett.* **103**, 242406 (2013).
- [33] J. Zhang, Y. Wang, X. Ding, Z. Zhang, Y. Zhou, X. Ren, K. Otsuka, J. Sun, and M. Song, Stress-induced strain glass to martensite (R) transition in a $\text{Ti}_{50}\text{Ni}_{44.5}\text{Fe}_{5.5}$ alloy, *Phys. Rev. B* **83**, 174204 (2011).
- [34] Y. Zhou, D. Xue, X. Ding, K. Otsuka, J. Sun, and X. Ren, High temperature strain glass transition in defect doped Ti-Pd martensitic alloys, *Phys. Status Solidi B* **251**, 2027 (2014).
- Correction:* An affiliation has been added for the seventh author, necessitating renumbering of affiliations for the eleventh and twelfth authors.